

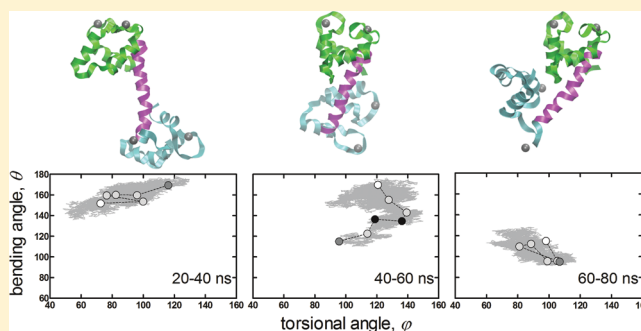
Calmodulin Readily Switches Conformation upon Protonating High pK_a Acidic Residues

Sunita Negi, Ayse Ozlem Aykut, Ali Rana Atilgan, and Canan Atilgan*

Sabanci University, Faculty of Engineering & Natural Sciences, Tuzla, 34956 Istanbul, Turkey

S Supporting Information

ABSTRACT: We investigate protonation as a possible route for triggering conformational change in proteins by focusing on the calmodulin (CaM) example. Two hundred nanosecond molecular dynamics (MD) simulations are performed on both the extended and compact forms of calcium loaded CaM. The stability of both structures is confirmed under prevailing conditions. Protonation of nine acidic residues with upshifted pK_a values leads to a large conformational change in less than 100 ns. The structure attained is consistent with fluorescence resonance energy transfer experimental results as well as structures from an ensemble compatible with NMR data. Analysis of the MD trajectories summing up to one microsecond implies that the key events leading to the completion of the conformational change begins with an initial formation of a salt bridge between the N-lobe and the linker, followed by the bending of the C-lobe and the organization of a stabilizing hydrophobic patch between the lobes. We find that CaM utilizes its Ca^{2+} ions to harden/soften different regions so as to achieve various conformations. Thus, barrier crossing between extended and compact forms of CaM which is normally a rare event due to the repulsive electrostatic interactions between the two lobes is facilitated by protonation of high pK_a residues. The results delineate how pH changes might be utilized in the cell to achieve different conformation-related functions.



1. INTRODUCTION

In the cell environment there is small copy number of the molecules involved in processes and short times are required for key events to occur. Moreover, external factors such as composition of the solvating environment quantified by pH and ionic strength, as well as the temperature affect the dynamical landscape of proteins. A quantitative characterization of ionization-coupled conformational transitions is yet to be developed, and recent advances in thermodynamical treatments have been made in this direction.¹ Therefore, studying the conformational changes in proteins, induced by various environmental factors remains to be challenging.

Here we focus on calmodulin (CaM) which plays a central role as an intracellular calcium ion receptor and in the calcium signaling pathways in the eukaryotic cells.² CaM can bind to a variety of other proteins or small organic compounds, and mediates different physiological processes by activating various enzymes.^{3,4} Reported crystal structures of CaM in free and bound forms to Ca^{2+} , proteins or small organic molecules indicates that this protein is capable of sustaining large conformational changes that are distinct to each interacting partner.^{2,4,5}

In a previous manuscript, we have studied the conformational changes calcium loaded CaM is prone to, using the perturbation-response scanning (PRS) method.⁶ PRS is based on the assumption that the equilibrium fluctuations at a given local energy minimum of the protein has the tendency to

convert to other viable conformations via a path that may be approximated linearly. Thus, characterizing the fluctuations by the Hessian matrix of the protein, single residue perturbations are inserted as forces and the resulting conformational change is calculated using linear response theory.⁷ By scanning the protein residue-by-residue, each in hundreds of possible directions, we determine the residue/force combinations that best represent the conformational change between open/closed forms of the protein under investigation. We find that in many cases, the response to single residue perturbations represents the conformational change,⁸ and may be used to uncover allosteric pathways.⁹ This coarse-grained method parallels in spirit the molecular mechanics-based scanning performed on all-atom representations of proteins, whereby perturbations are inserted as displacements rather than as forces.¹⁰

For the particular case of CaM,¹¹ as well as a bacterial iron transport protein,⁶ PRS reveals that the residues whose perturbation yields the experimentally observed conformational change upon ligand binding are those for which pK_a values are shifted into the physiological range.¹² Dynamical information obtained from fluorescence resonance energy transfer (FRET) experiments measuring the distance distributions between labeled sites residing on separate lobes of Ca^{2+} -CaM show

Received: April 6, 2012

Revised: May 15, 2012

Published: May 24, 2012

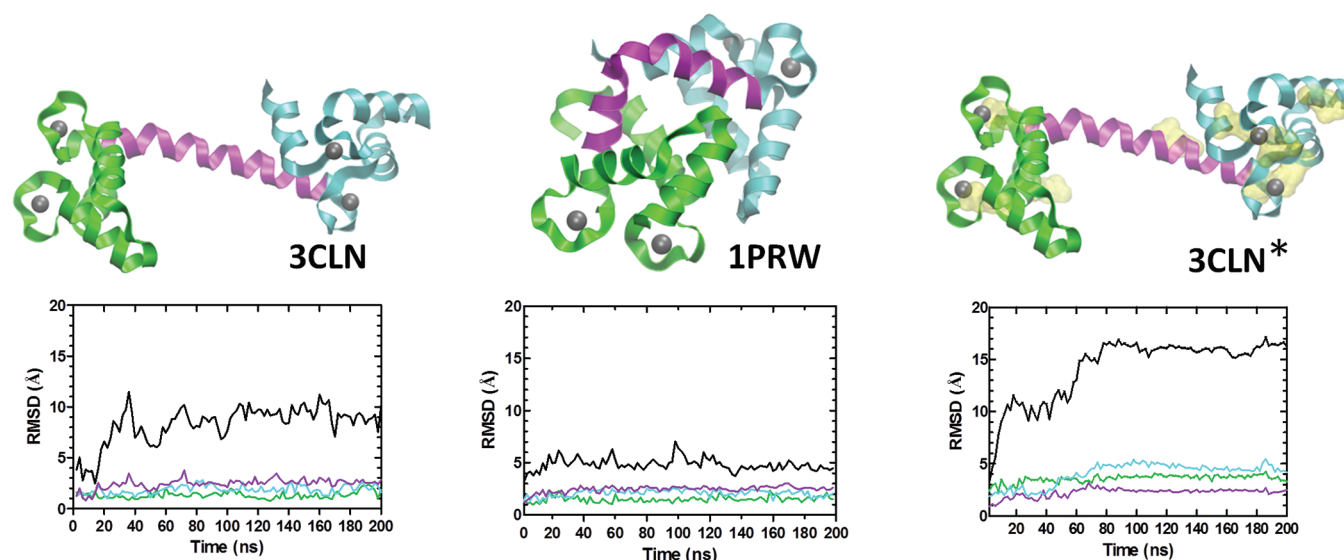


Figure 1. Initial structures of the simulations and rmsd of the protein trajectory for the 3CLN, 1PRW and 3CLN*. Top panel: The three regions are colored so that N-lobe, linker and C-lobe are shown in green, purple, and cyan, respectively. Ca²⁺ ions are shown as gray spheres. In 3CLN*, protonated residues are shown in yellow transparent surface representation. Bottom panel: rmsd of the whole protein shown in black, as well as the rmsd of the three regions color coded in parallel with the top panel.

that not only do at least two separate conformations exist in solution under physiological conditions, but that the equilibrium is shifted toward a single, more compact form upon decreasing the pH from 7.4 to 5.0.^{13,14} Furthermore, the time scale for conformational switching has been determined to be on the order of 100 μ s.¹⁵ Other experimental work also investigates the dynamic nature of CaM conformations. 1.0 Å crystal structure of Ca²⁺–CaM provides evidence for domain displacements and discrete backbone disorder, suggesting that it occupies a number of hierarchical set of substates even in the crystal.¹⁶ More recently, pseudocontact shifts and residual dipolar couplings of the C-terminal domain obtained using nuclear magnetic resonance (NMR) showed that neither the dumbbell-shaped conformation observed in early crystal structures of the molecule,¹⁷ nor the compact conformation determined later on³ is consistent with the conformations sampled in solution. All these experimental data identify CaM as a protein which samples multiple conformations; they also distinguish the shifts in the distribution of their populations by changing environmental conditions, such as pH, Ca²⁺ concentrations, and ionic strength (see ref 11 and references cited therein). None, however, directly identifies the particular conformations sampled by the protein. They also cannot describe the events occurring along the path sampled between different conformational states.

In this work, we investigate the range of conformations sampled by Ca²⁺–CaM using extensive molecular dynamics (MD) simulations. There is indeed other work where different aspects of CaM dynamics have been studied by using MD as a tool. The fully loaded CaM structure was studied in a 44 Å sphere of water for 3 ns using the CHARMM force field at 150 mM ionic strength (IS)¹⁸ and in the NPT ensemble for 4 ns CHARMM at 150 mM IS¹⁹ or for 11.5 ns using the AMBER99 force field at 70 mM IS.²⁰ In all three studies, the flexibility of the linker was reported as the most important result, postulated to lead the reorientation of the two domains into a position favorable for target binding. Original ¹⁵N NMR measurements of the backbone dynamics of Ca²⁺–CaM indicate a very high

degree of mobility for the linker residues 78–81.²¹ As a result of the conformational variability of the linker, the radius of gyration readily decreases from 22.0 Å of the original X-ray structure to a value of 21.5 ± 0.5 Å under CHARMM22 force field at 60 mM IS.²² In fact, the flexibility of the linker has been studied as an intrinsic property as opposed to being a result of the presence of the two lobes attached to it. Three nanosecond long MD simulations using the CHARMM force field were conducted only on the linker region and bending motions operating on the 0.5 ns time scale were observed.²³ The coupling between bending and torsional modes of the linker was further demonstrated by Monte Carlo methods.²⁴ In our recent work where 120 ns MD trajectories were generated with the CHARMM force field at relatively low IS, wide conformational freedom around the linker with $\pm 20^\circ$ in the bending angle accompanied by large twisting motions was recorded, corroborating these earlier work on much longer time scales.¹¹ Note that all the above-mentioned studies utilized the TIP3P water model.

It has also been established, based on 4 ns long trajectories produced under the AMBER force field and SPC water model at 80 mM IS, that the presence of coordinated calcium ions decreases the flexibility of CaM. Even the removal of a single Ca²⁺ ion from the N-lobe resulted in compaction of the extended initial structure within 7.5 ns in a 12.7 ns trajectory. In the latter work, the trajectory generated by the GROMOS96 force field with SPC water at 200 mM IS was compared with a fully Ca²⁺ loaded control trajectory where the conformational change does not occur.²⁵ Further, a coupled MD – molecular mechanics approach operating under the AMBER force field and TIP3P water model leads to the fast propagation of the intradomain conformational changes obtained upon removal of all Ca²⁺ ions where the method is applied separately to either the N- or the C-domain.²⁶

Thus, independent of the water model, force field type or IS values used, previous studies point to the stability of the extended form of fully Ca²⁺ loaded CaM, despite the high degree of flexibility observed in the linker. One study offers a

different observation in that within 5 ns of a 20 ns long MD simulation under the GROMOS force field in SPC model, the extended crystal structure adopts a compact conformation similar to those of CaM in complex with target peptides, while a substantially different orientation between the N- and C-domains remains.²⁷ The authors offer as an explanation the low IS employed in that work (25 mM) compared to the previous ones. Yet, our 120 ns long simulations, also carried at relatively low IS, lack the large conformational change.¹¹ The reason for the discrepancy might be due to the increased mass of hydrogen atoms in CaM adopted to enable 4 ps time steps which might have affected the screening of charges by water in this heavily charged protein.

Motivated by our previous work where acidic residues with upshifted pK_a values are implicated in conformational change,¹¹ here we make a systematic study of the dynamics of Ca^{2+} –CaM on time scales up to 200 ns for three separate initial configurations. Two of these employ the extended and compact forms of CaM, and assign the standard charge states of the residues. In the third set, the extended structure of Ca^{2+} –CaM is modified by changing the protonation states of nine residues, so as to mimic the most probable charge states of residues at pH 5. For each system, a basis 200 ns simulation is performed and second independent runs up to 200 ns is carried out to ensure the repeatability of the findings. We find that while the deprotonated Ca^{2+} –CaM structures are stable under the prevailing conditions, protonated CaM undergoes a large conformational shift on the time scale of tens of nanoseconds that leads to a relatively more compact form. Fluctuation patterns and dominant modes of motion help identify if the system is prone to a large conformational change. We argue the conformations attained are experimentally relevant and we analyze the key events that lead to the final compact conformation in protonated CaM.

2. MODELS AND METHODS

2.1. Calmodulin. CaM consists of 148 amino acids made up of the N-lobe (residues 1–68), the central linker/helix (residues 69–91) and the C-lobe (residues 92–148). Apo-CaM is free of calcium ions. Ca^{2+} ions activate CaM to interact with other proteins; holo-CaM is fully loaded with four calcium ions.²⁸ Fully loaded CaM free of other ligands has two distinct experimentally determined conformations: In many X-ray structures, CaM has an open form with a dumbbell shape containing two domains, joined by an extended linker. It is exemplified by the Protein Data Bank (PDB)²⁹ structure 3CLN.¹⁷ Another form is compact, whereby the central linker is bent (PDB code 1PRW³); these are shown in the top panel of figure 1. Each of the N- and the C-lobes holds two calcium ions in their respective EF-hand motifs. The coordinating residues in each of the four EF-hands are D20-D22-D24-E31 in loop I, D56-D58-N60-E67 in loop II, D93-D95-N97-E104 in loop III, and D129-D131-D133-E140 in loop IV.

2.2. Simulation Details. Three sets of simulations are performed with the following initial structures: (a) the extended form with all residues assigned their standard protonation states, (b) the compact form with all residues at the same protonation states as in (a), and (c) the extended form where nine residues are protonated (3CLN*). These sets are labeled 3CLN, 1PRW and 3CLN* throughout the text. The selection of protonated residues in 3CLN* is described in the next subsection.

All the simulation sets are performed for 200 ns. In addition, we have performed independent runs to check the reproducibility of the results (100 ns for 3CLN and 3CLN*, 200 ns for 1PRW). The coordinates of residues 1–4 and 148 are not included in the 3CLN and 3CLN* runs as their coordinates are not reported in the X-ray data. We use the NAMD package to model the dynamics of the protein-water system.³⁰ The protein is soaked in a water box of at least 10 Å from all directions using the VMD 1.8.7 program with solvate plug-in version 1.2.³¹ The CharmM27 force field parameters are used for protein and water molecules.³² Water molecules are described by the TIP3P model. The initial boxes have dimensions $63 \times 89 \times 71$, $60 \times 59 \times 62$, $72 \times 92 \times 72$ Å containing 37099, 20330, and 31660 atoms in the 3CLN, 1PRW, and 3CLN* simulations, respectively, neutralized by standard addition of ions. Long range electrostatic interactions are calculated by the particle mesh Ewald method,³³ with a cutoff distance of 12 Å and a switching function at 10 Å. RATTLE algorithm³⁴ is applied to use a step size of 2 fs in the Verlet algorithm. Temperature control is carried out by Langevin dynamics with a damping coefficient of 5/ps. Pressure control is attained by a Langevin piston. Volumetric fluctuations are preset to be isotropic. The system is run in the NPT ensemble at 1 atm and 310 K until volumetric fluctuations are stable to maintain the desired average pressure. The respective box dimensions of equilibrated structures in the 3CLN, 1PRW and 3CLN* are simulations $62 \times 87 \times 69$, $58 \times 57 \times 60$, $64 \times 81 \times 60$ Å. The resulting respective ionic IS are 76, 147, and 43 mM. Thus, the 3CLN and 3CLN* runs are at low IS, while 1PRW run is at nearly physiological IS. The run in the NPT ensemble is then extended to 200 ns for data collection stage. The coordinate sets are saved at 2 ps intervals for subsequent analysis, leading to 100 000 snapshots.

In a series of studies of calbindin dynamics, force field differences were reported as sources of deviations from experimental observations.^{41,42} Ca^{2+} ion parameters were questioned as possible sources of error, and the behavior of Ca^{2+} –protein association was monitored for GROMOS96 and OPLS-AA force fields.⁴¹ The findings implied that the GROMOS96 force field might have too weak carboxylate– Ca^{2+} parameters to dismiss the water shell around the ion to form direct association with the protein; the reverse was observed to be the case for OPLS-AA where the strong interactions do not lead to occasional dissociation of the ion from the protein. Moreover, MD simulations for single aspartate amino acid and Ca^{2+} in water were carried out, leading to the same observations in the absence of the strongly charged protein. In the latter simulations, CHARMM22 force field was also included and was observed to display similar qualitative behavior to GROMOS96. We have therefore monitored all our trajectories to see if Ca^{2+} –protein interactions are too weak to overcome the water bridges. We find that there is equilibrium between direct contact and water-mediated association. A snapshot of the EF-hand motif 1 is displayed at the final step of the 3CLN* simulation in Supporting Information Figure S1, where there are no water molecules within 5 Å of the Ca^{2+} ion. Sample distance profiles of Ca^{2+} ion and aspartic acid residues in each of the four EF-hand motifs are displayed in Supporting Information Figure S2. The direct contact distance is ~ 2.2 Å, and water mediated association of the ion occurs at distances as much as 4.5 Å. Thus, we conclude that the force field provides an adequate representation of carboxylate– Ca^{2+} interactions.

2.3. Selection of Protonation Sites. For the 3CLN*, the protonation states of the residues are determined so as to select the most probable state of each ionizable residue at pH 5. Four different servers H^{++} ,^{35,36} pK_a ,^{37,38} $propKa$ 3.1,³⁹ and PHEMTO⁴⁰ are used to calculate the pK_a of all the titratable groups. The pK_a values calculated for all the titratable residues are listed in Supporting Information Table S1. There are a total of 52 such sites in CaM, two of which are Tyr with high pK_a values, and one His which we take to be uncharged in all simulations. The standard error on the mean of the remaining Glu/Asp/Arg/Lys residues is calculated to be less than 0.5 units in 34 cases, and less than 1.3 units for 44 cases. In the remaining five, the residues are either consistently protonated above pH 5 (e.g., for residue Glu 67, we have $pK_a = 11.2$, 5.4, 13.4 and 8.5, respectively for H^{++} , pK_a , $propKa$ 3.1 and PHEMTO) or they are deprotonated for at least three of the four pK_a predictors. This lets us assign the protonation states consistently. We find that the acidic residues 11, 31 (loop I), 67 (loop II), 84, 93 (loop III), 104 (loop III), 122, 133 (loop IV), and 140 (loop IV) are consistently upshifted in pK_a from the standard values of ~ 4 –5.5 or more. Out of these nine residues 11, 31, and 67 are on the N-lobe, 84 is on the central linker, and the remaining five residues are on the C-lobe; these residues are highlighted in transparent yellow (top panel, 3CLN* in Figure 1). All other negatively charged residues are near their standard pK_a values in the protein environment, so that they are kept in the charged state throughout the simulation. None of the positively charged residues have downshifted values, and their protonation states are also unaltered. We note that, although six residues in EF-hand loops are protonated, none of the Ca^{2+} dissociate into the water in any part of the simulations.

2.4. Modal Analysis. Throughout the text, the term “mode” refers to principal components of the covariance matrix obtained from MD trajectories. The covariance matrix of atomic fluctuations, C , is obtained from a suitable length of the MD trajectory (40 ns in this work). To determine the collective modes of motion, we decompose the covariance matrix as $C = U^T \Lambda U$ where Λ is a diagonal matrix whose elements λ_i are the eigenvalues of C , and U is the orthonormal matrix whose columns u_i are the eigenvectors of C . C has six zero eigenvalues corresponding to the purely translational and rotational motions. To assess the similarity of the modes obtained from different trajectories, we use the overlap measure,

$$O_{ij} = \frac{u_i \cdot u_j}{|(u_i \cdot u_i)(u_j \cdot u_j)|^{1/2}} \quad (1)$$

To measure the convergence of the trajectories, we have studied the spectral properties of the covariance for (i) the first 40 ns portion, (ii) the last 40 ns portion. In each case, the average structure belongs to that portion of the trajectory analyzed and for each residue positional deviations are measured according to the average structure. We check that the contributions of each eigenvector to the overall spectra converge in these trajectories. We also note that the first five eigenvectors account for more than 96% of all the motions in each case.

3. RESULTS AND DISCUSSION

The effect of solution conditions, such as IS and pH, on the distribution of conformational substates of CaM, as well as the submillisecond dynamics has been determined previously by single-pair FRET experiments.⁴³ The size distributions of the

Ca^{2+} –CaM molecules are found to be dependent on solution conditions. At pH 7.4, at least two major populations are postulated, based on the distance distributions between tags on residues 34 and 110, residing on the two lobes of CaM. The two ranges are centered around 34 and 55 Å, with an average value of 37.2 ± 0.3 Å. At the reduced pH, not only does the average value decrease to 31.5 ± 0.4 Å, but also there is only a single apparent population, under conditions where the spectroscopic properties of the acceptor such as lifetime, quantum yield and anisotropy are unchanged. The dynamics of jumps between conformational substates occur on 100 μ s time scale at 7.4 pH.¹⁵ On the basis of these observations, the conformational switching is not expected to be observed on the time scales reachable by conventional all atom MD simulations at physiological pH. Furthermore, the system is expected to evolve toward a single equilibrium state at low pH.

Here, we study the system starting from the two experimentally determined open and closed conformations (3CLN and 1PRW). No conformational jump between open and closed states are observed for 200 ns in either system. Protonating nine residues so as to mimic the most probable states of acidic residues at pH 5 leads to a closed conformation in less than 100 ns. Below we describe and interpret the MD simulation results.

3.1. rmsd of the Trajectories. The root-mean-square distances (rmsd) of the different parts of the protein are compared to the original structure in the bottom panel of Figure 1. In the 3CLN run, the rmsd of the protein increases to ~ 10 Å within 30 ns, and keeps this level for the rest of the simulation. Initially, the constraints imposed on this highly charged protein by crystal packing are relieved in solution. However, neither the locations of the Ca^{2+} ions, nor the overall structure of the N-lobe, C-lobe, or the linker is changed during the course of the simulations, as may be seen from the separate rmsd values of these regions (figure 1, bottom panel, left). The linker does display a somewhat larger degree of conformational fluctuations compared to the N- and the C-lobes, as outlined in the Introduction.^{18,20–22} For 1PRW (Figure 1, bottom panel, center), the overall fluctuations are smaller on average compared to 3CLN with a value around 5 Å. This is due to its compact structure; although this structure also moves away from its X-ray coordinates initially, the three regions act in a more coordinated fashion. The individual rmsd of the N- and C-lobes, as well as the linker, are similar to that of 3CLN.

In 3CLN*, we see a different pattern in rmsd. The overall conformation of the chain changes in two steps, first at ~ 15 ns, then at ~ 65 ns, while the rearrangements within the different units are relatively small (Figure 1, bottom panel, right). Thus, the main conformational change is due to the relative arrangement of the units with respect to each other. Inspecting this figure more closely, though, we find that the C-lobe motions are relatively larger, while the linker maintains its original helical structure, but is observed to be slightly bent at some instants. The latter point is important, because various authors have argued that the loss of the helicity in the central linker might be the source of the conformational multiplicity of CaM.^{20,22,27}

A close up of the linker conformations collected throughout the simulations are displayed in Figure 2. The average rmsd of the linker is on the order of 3–4 Å in each case. In both 3CLN and 3CLN*, the initially extended linker does not sample bent conformations, despite the large degree of fluctuations accompanied by local unfolding events. Similarly, the bent

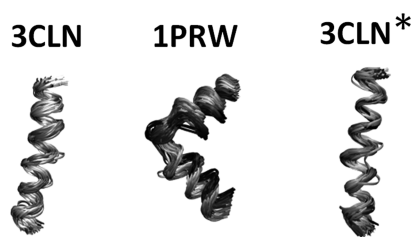


Figure 2. Linker conformations adapted during the MD simulations. Snapshots collected at 2 ns intervals are displayed, yielding a total of 100 superimposed structures.

1PRW linker structure is also stable throughout the simulation. However, the motions in 3CLN and 1PRW carry bending and torsional modes, as was discussed in detail in our previous work.¹¹

3.2. Relative Bending and Torsional Motions of N- and C-Lobes. To capture the main features of the relative motions of the two lobes and the linker, we reduce the CaM structure to five points in space as in our previous work.¹¹ These points are schematically shown in Figure 3a. Three of these are the center of masses (COMs) of the N-lobe (point 1), C-lobe (point 5), and the linker (point 3). In addition, residues 69 and 91 are used to mark the beginning and end points of the linker (points 2 and 4). We then define two main degrees of freedom to capture the essence of the motions of the two lobes relative to each other. θ angle defines the bending motion observed between the N and C lobes, and φ angle defines the relative rotation of the two lobes around the linker as a virtual

dihedral angle. The (θ, φ) distributions are shown in Figure 3b. The bending angle in 3CLN and 1PRW runs is restricted to their respective narrow intervals of $160 \pm 20^\circ$ and $100 \pm 20^\circ$. The torsional angle of the extended 3CLN structure spans a large interval leading to the high rmsd fluctuations (10 Å) of the protein structure observed in figure 1. This hints at the presence of an energetic barrier in the bending angle which neither of the native deprotonated forms is able to circumvent under prevailing conditions.

We find that the energy landscape is sufficiently altered by protonating the selected residues in 3CLN*. Figure 3b (purple) shows that the extended starting structure samples the same region as 3CLN in the initial phases of the simulation, also providing a similar rmsd in the 10 Å range. This is followed by crossing over the barrier leading to the same bending angle range as the 1PRW system, with a somewhat lower torsional angle value. The 3CLN* run is detailed in figure 3c. During the first 40 ns the bending angle covers a relatively restricted region of values ($140\text{--}180^\circ$), while the torsion angle is more flexible ($60\text{--}140^\circ$). At ~ 55 ns, the bending motion is realized for the first time, following a critical torsional motion. The completion of the transition takes ~ 20 ns, also observed as a step in rmsd values from 10 to 16 Å; however, the actual crossing over event takes as short as 100 ps. By ~ 80 ns, the bending angle value is ca. 110° implying a closer association of the N- and C-lobes. By 100 ns, the bending angle may get as low as 90° . For the last 80 ns, the protein is observed to attain a stable point where the $(\theta, \varphi) = (100 \pm 10^\circ, 100 \pm 20^\circ)$.

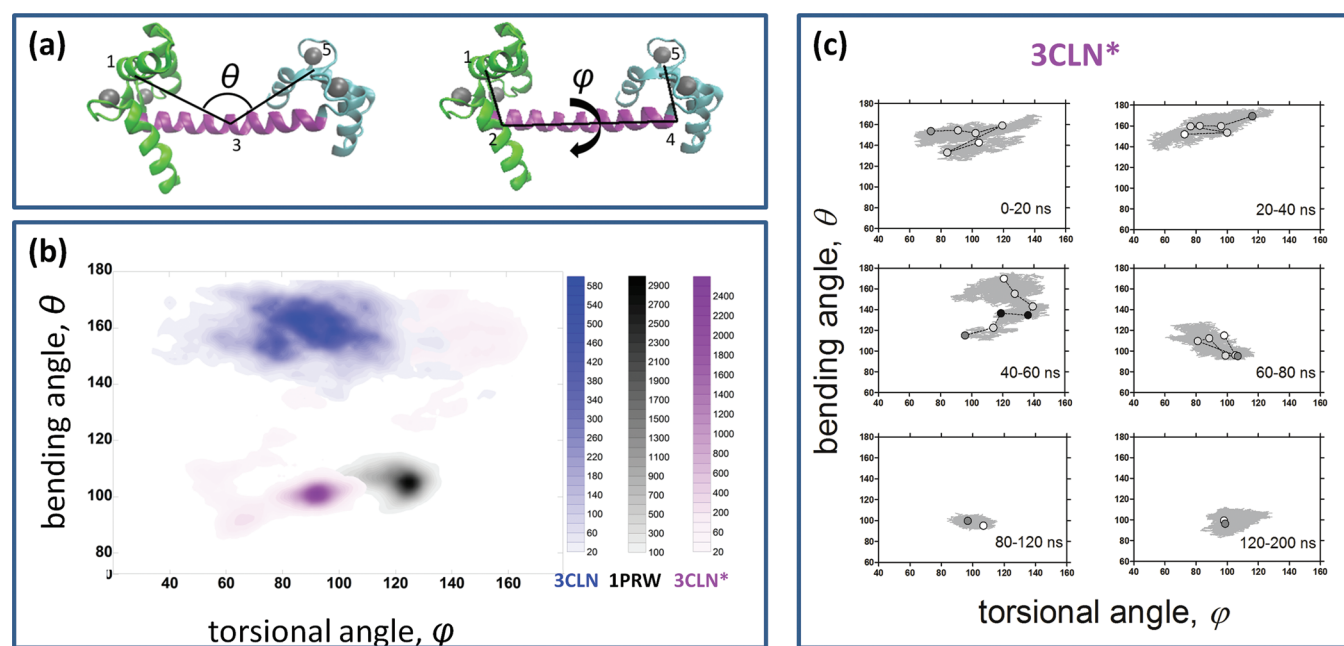


Figure 3. (a) Reduced degrees of freedom are defined as the bending (θ) and torsion (φ) of the two lobes around the linker. (b) Sampling of the (θ, φ) regions by the different configurations: 3CLN (blue) samples a wide range of torsions while it has a confined region for the bending of the lobes. Thus, the two lobes are placed far from each other, in an extended conformation, despite their large conformational freedom. 1PRW (grayscale) is restricted to a more narrow part of the conformational space where both the angles display $\pm 20^\circ$ fluctuations around their average values. 3CLN* (purple) starts out by sampling a region overlapping with that of 3CLN. It then finds a route to the compact form and samples a restricted region once it completes the conformational jump from the extended to the compact form. Scale bars indicate counts and total 100000 for each trajectory. (c) Detailed (θ, φ) trace of the 3CLN* run. The trajectory up to 80 ns is divided into 20 ns ranges (0–20, 20–40, 40–60, 60–80 ns), and the last two parts is divided into larger regions (80–120, 120–200 ns). All sampled points are displayed in gray, initial and final conformations of each chunk are marked by a full white and full dark gray circle. Other, 4 ns distant points are also marked up to 80 ns. Finally, the transition state is marked by the black circles in the 40–60 ns trajectory piece, where the two points are only 100 ps apart.

3.3. Modal Analysis. We use the collective modes to classify the types of motion experienced by the structure in the different MD runs (see section 2.4). We use the first 40 ns portion of the 3CLN and 1PRW simulations to calculate the covariance matrices representing the fluctuation behavior of the residues. Using the whole trajectory smears out the information embodied in separate modes due to the sampling of larger conformational energy wells and the resulting interlacing of the modes.^{12,44} The 3CLN* run is expected to be more similar to the 3CLN run in its initial parts, and to the compact form 1PRW after equilibration. Thus, we use the first 40 ns of the 3CLN* run to compare the structural features of the open form obtained in this run with the equilibrium 3CLN structures sampled. Similarly, we use the final 40 ns portion of the 3CLN* run to compare the newly obtained closed structure with 1PRW.

The dominant mode in 3CLN is the simultaneous twist/bend motion around the linker, as discussed previously.¹¹ That of compact 1PRW is a breathing-like motion, expanding around the bent linker (not shown). In both cases, the most dominant mode is well separated from the rest, contributing over 50% of the motion, as measured by the quantity ($\lambda_i/\Sigma\lambda_j$). Accordingly, the analysis of the motions around the equilibrium states of the X-ray structures imply that the open structure has a clear propensity to close. Conversely, the closed form does not constitute a hinge-like opening motion. Considered together with the sampling of the reduced conformational space displayed in Figure 3b, the 1PRW structure is constrained to a small portion of the conformational space, possibly separated from the rest of the structures by large potential energy barriers.

In Figure 4, the slowest mode shape is displayed for 3CLN*, obtained from the initial and final parts of the trajectory. Their overlap (eq 1) and contributions to the overall motion is summarized in Table 1. We note that the first 40 ns of this run corresponds to a transient state; nevertheless, its lowest frequency mode, which contributes 41%, is expected to capture the directionality of the motion involved, eventually leading to

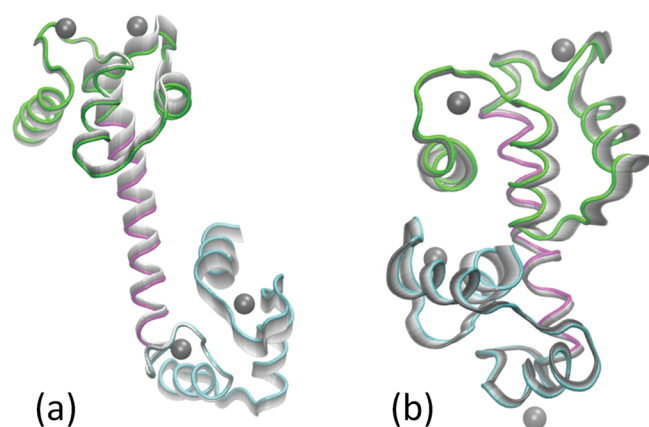


Figure 4. Most collective mode shape of 3CLN* calculated from the covariance matrix obtained from the (a) initial 40 ns and (b) final 40 ns portions of the trajectory. The directionality of motion is from the darker toward the lighter shades of gray. The N-lobe, linker and the C-lobe are colored as in figure 1. In a, a compressive motion on the linker is present; it is especially dominant in the region closer to the N-lobe. In contrast, in b, the linker is nearly immobile. The mode in (b) describes opening–closing motion of the two lobes. The structures look distorted since the mode shape is superimposed on the average coordinates obtained in the 40 ns portion studied.

Table 1. Overlap of First Five Modes Obtained from the Initial and Final Parts of 3CLN* Trajectory^a

mode number	3CLN* (closed)				
	1 (34)	2 (13)	3 (12)	4 (9)	5 (8)
3CLN* (open)					
1 (41)	0.05	0.17	0.24	0.03	0.57
2 (15)	0.12	0.19	0.52	0.13	0.23
3 (13)	0.31	0.06	0.27	0.29	0.19
4 (10)	0.10	0.43	0.43	0.24	0.10
5 (9)	0.27	0.12	0.20	0.58	0.04

^aPercent contribution of the mode to the overall motion ($\lambda_i/\Sigma\lambda_j$) is given in parentheses.

the conformational change. This mode is dissimilar to the lowest frequency mode of 3CLN, with only 0.33 overlap. It lacks the simultaneous twist and bend, but rather constitutes an accordion-like motion which is particularly compressive around the linker region. With 0.70 overlap, it is quite similar to the fourth slowest mode of the 3CLN system which contributes only 9% to the overall motion at equilibrium. Thus, while the 3CLN structure carries this accordion like motion, its contribution is only accentuated when the nine residues are protonated in 3CLN*. Perhaps more important, the simultaneous twist/bend motion is an inherent property when there is the strong charge distribution on the opposite lobes of the protein. This mode is absent when the charge distribution is milder so that it is possible to bring together the partially positively charged region on the N-lobe with the highly negatively charged region on the C-lobe more directly.

The modes obtained from the last 40 ns of the trajectory describe the motions in the equilibrated final structure. Unlike 1PRW, the slowest modes all describe opening up of the CaM structure. In fact, there is no similarity between these and the 1PRW modes (the maximum overlap is 0.44 for mode 3). The similarity between the modes obtained from the initial and final parts of the 3CLN* trajectory is also relatively low and their sequence of appearance is reshuffled as shown in Table 1; therefore, the two ends of the simulation describe completely different dynamics.

Although the 3CLN* system initially samples similar regions of conformational space with the 3CLN system (Figure 3b), the modal analysis displays that the motions involved are qualitatively very different, eventually producing the conformational jump leading to the closed form. It further quantifies how the closed structure obtained is different from the 1PRW structure. Finally, the 1PRW structure is shown to display no propensity to open, while 3CLN attempts to sample closed conformations via simultaneous bending and twisting motions around the linker.

3.4. Relevance of Sampled Conformations to Experimental Observations. Conformational variability of CaM under different conditions has been the subject of many studies. FRET findings, detailed in the opening of section 3, provide dynamical information on the changes occurring in conformational distributions under different environmental conditions. We present the 34–110 residue distances calculated from the three sets of MD simulations in figure 5a. While the 3CLN structures are peaked around 40 Å, the 1PRW set is compact, with 34–110 distances centered on 14 Å. Such very compact structures are not sampled in FRET experiments either at low or high Ca^{2+} concentrations, nor at pH 7.4 or 5.0.⁴³ Some compaction of the sampled structures with decreased pH in Ca^{2+} -CaM is observed in the FRET measurements; moreover,

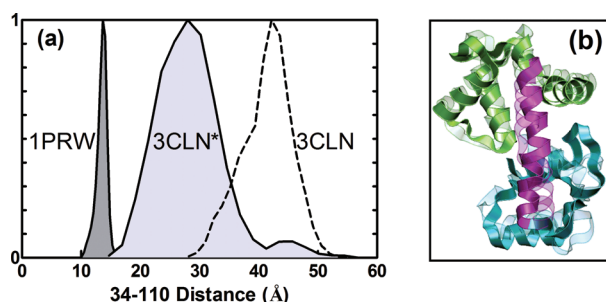


Figure 5. (a) Cumulative distribution of the distance between Ca atoms of residues 34 and 110. Each curve is normalized by equating the largest bin to 1. (b) Superposition of an equilibrated sample structure of the 3CLN* system and the closest NMR compatible structure from among those reported in ref 49.

reduced pH stabilizes the conformations sampled. In accord with FRET observations, in the 3CLN* system where protonation states of residues is selected such that acidic residues are assigned their most probable values at pH 5, relatively more compact structures are sampled, even before the conformational switch discussed in section 3.2 occurs at 67 ns. The maximum of the 3CLN* curve in figure 5a occurs at 28 Å, reduced from the 40 Å of deprotonated 3CLN system.

While FRET studies present information on conformational distributions, these are coarse measurements with sensitivity on the order of hundreds of μs time scales and providing distances between a pair of labeled sites. The study of conformational multiplicity in CaM has also been the subject of NMR studies which provide more direct information on the conformations through the use of residual dipolar couplings (RDCs) and pseudocontact shifts. This information not only yields structural detail,⁴⁵ but also gives information on the maximum likelihood of observing certain structures.⁴⁶ As with the FRET results, using the RDCs clearly show that the closed structures exemplified by 1PRW and several other peptide bound structures are rarely sampled in solution.^{13,14} For example, the maximum occurrence (MO) of the closed crystalline form has MO of only 5% and compact conformations in general have small MOs.⁴⁷ In fact, minor compact conformations visited up to 10% of the time have been examined in detail by NMR using paramagnetic relaxation enhancement (PRE).⁴⁸ The fully extended structure, on the other hand, has 27% MO, while the conformation exemplified by the PDB structure G4Ys where the protein adopts a less compact conformation with respect to 1PRW and other CaM-peptide complexes by the extension of the CaM linker region has 31% MO.⁴⁶ The latter is similar in description to the final structure obtained in 3CLN*.

We have compared the average structure obtained over the last 40 ns of the 3CLN* simulation with the 160 structures obtained by MD simulations where Nuclear Overhauser Enhancement and order parameter (S^2) data from NMR experiments are used as restraints (PDB code 2K0E).⁴⁹ We note that while these are structures consistent with the NMR data used in their generation, it is possible to further restrict the conformational space explored by using additional experimental information including RDCs, small-angle X-ray scattering data.^{47,48} In Figure 5b we display a representative structure of the 3CLN* equilibrated conformation (at 189 ns in this case) compared with one of the best-fitting structures from the NMR-related ensemble. The overall backbone RMSDs of these structures is 5.4 Å, with N-lobe only and C-lobe only rmsd of

3.3 and 4.3 Å, respectively. The relative orientations of the secondary structural elements are the same in the two cases. The main source of the difference comes from the relatively flexible EF-hand motif loops and the linker which is partially bent in the NMR structure, while it is almost straight in the 3CLN* structure.

3.5. Role of Electrostatics on the Conformational Change.

The Ca^{2+} -CaM structure has to perform a simultaneous twisting and bending motion of the two lobes to overcome the energy barrier between the open and closed structures, exemplified by the 3CLN and 1PRW X-ray structures. In fact, the dominant mode calculated from the 3CLN MD simulation accommodates this motion.¹¹ However, the transition from the extended Ca^{2+} -CaM structure to the one with a bent linker is not likely to occur, unless there is a ligand clamped by the two lobes screening the interaction of the two domains (see, for example, CaM-myosin light chain kinase complex⁵⁰). We note that many of the liganded structures of Ca^{2+} -CaM have low rmsd with 1PRW; for example, 4.2, 3.6, 5.2, and 4.6 Å rmsd with 1LIN, 1QIW, 2BBM and 1CDL, respectively.¹¹ Thus, although 3CLN dynamically has the propensity to complete the conformational change, the motion is prevented due to the large electrostatic repulsions between the two lobes which are predominantly negatively charged. However, in Ca^{2+} -CaM, as opposed to apo-CaM, there is also a partially positively charged region on the N-lobe.⁴⁸ Yet, the extended structure must perform the suitable motions to bring together this patch with the highly negatively charged C-lobe. That the interdomain PREs in Ca^{2+} -CaM depend on salt concentration lends support to the role of electrostatics on compaction.⁴⁸

To check if one may encourage the system to overcome the barrier separating the two structures, we have performed a series of steered MD simulations whereby the molecule was perturbed from a series of different locations in different directions and magnitudes (data not shown). We find that, while the system first follows the path of the MD trajectory along the torsional angle degree of freedom described in section 3.2, the bending is prevented by a large force of electrostatic origin. The regions sampled are limited to those sampled by the 3CLN run. Further perturbations in any direction increase the interaction energies drastically, implying that the barriers are high.

Protonation of the nine residues in the 3CLN* system does not lower the barrier, but creates an alternative path for the closing of Ca^{2+} -CaM. We calculate the interaction energy between the N- and the C-lobes using the NAMD energy plugin in VMD (Figure 6). The electrostatic interactions are observed to make the major contribution to the nonbonded energy while the van der Waals part is observed to be an order of magnitude smaller. A dip in the energy occurs around 40 ns followed by two large dips at 67 and 120 ns. After 120 ns, the lobe-lobe energy enters an increasing trend for ca. 20 ns, and stabilizes thereafter. To associate the main events taking place during the conformational change with the interlobe energetics, we study the interactions between residues in the protein throughout the simulation. The first key interaction that leads to the permanent shrinkage of the distance between the two lobes is a salt bridge between the N-lobe and the linker (E7 – R74) formed permanently at 40 ns. We attribute the first significant reduction in the lobe-lobe interaction energy to the stabilizing effect of this salt bridge which also restricts the motions of the N-lobe. The transition state occurs at ca. 55 ns

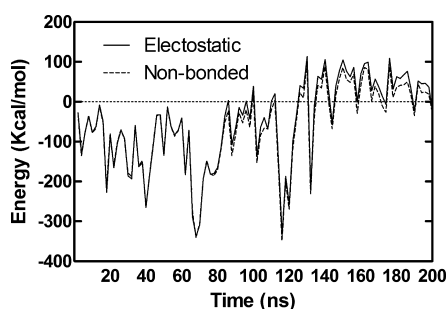


Figure 6. Nonbonded interaction energy between N and the C-lobes throughout the MD simulation. Most contributions come from the electrostatic component (dashed line), displaying that the van der Waals term has negligible effect on the conformational change.

with 20° swinging in the virtual torsional angle φ within ~ 100 ps (recall figure 3c). This event changes the relative placement of the two lobes from that of opposite directions with respect to the linker to the same side (compare the average structures in Figure 4a and b). At 67 ns, the calcium ion in the third EF-hand motif partially dissociates. This region, located in the C-lobe, immediately following the linker, partially unfolds after this event and lets the C-lobe approach the N-lobe. The major cause of enhanced C-lobe dynamics is that the protonated E104, which is part of the EF-hand motif III, weakens the grip of the motif on the Ca^{2+} . This is also the reason why the C-lobe attains a higher rmsd value than both the linker and the N-lobe from this point onward (recall Figure 2). The overall result of the loosened motif is the association of the C-lobe with the N-lobe which causes another dip in the energy. We note, however, that none of the Ca^{2+} completely dissociates from their EF-hand motifs in any portion of the simulation.

By 80 ns, the structure is further stabilized by the formation of a hydrophobic patch at the N-lobe–C-lobe interface. This event is accompanied by the raise in the interaction energy in the time range of 67–80 ns. Meanwhile, the C-lobe loosened at the EF-hand motif III performs a conformational search for a suitable region to latch on the rigidified N-lobe–linker. At 120 ns, the calcium ion of the EF-hand motif 4 is shared between the two lobes, held in place by two negatively charged residues from the linker and the C-lobe, E84 and E139. However, this is a transient event, and in the last 40 ns, the structure attains its stabilized form, shown in Figure 5b compatible with an NMR structure.

We also monitor the repeatability of the structural change by an independent simulation for 100 ns and have observed a similar compaction of the overall structure (see Supporting Information Figures S3–S5). The conformational change in fact happens faster in that instance, and is again initiated by the formation of a salt bridge between the N-lobe and the linker. The distribution of the 34–110 distances are similar to run 1 (Supporting Information Figure S4). Furthermore, even closer structures than those attained in run 1 to the NMR ensemble of ref 49 is attained (Supporting Information Figure S5). Thus, it appears that protonation of the nine residues, selected so as to mimic the most probable states of charged residues at pH 5, shifts the energy landscape such that the extended form is no longer preferred. A slightly more compact form is attained by first rigidifying the N-lobe–linker region by the formation of a salt bridge. While the linker keeps its helical structure, the EF-hand motif immediately following the linker operates as the conformationally flexible region searching for a suitable position

to stabilize the structure by bringing together the partially positively charged region on the N-lobe with the highly negatively charged region on the C-lobe. We emphasize, however, that these observations do not preclude other possible compaction events that may utilize the bending of the linker under different environmental conditions. We finally note that the observed time table of events may be influenced by force field and water model differences.

4. CONCLUSIONS

Conformational multiplicity of CaM has been the subject of numerous studies (see, for example, refs 47 and 48 and references cited therein). Those states populated by CaM under different environmental conditions enhance our understanding of the role of conformational selection and induced fit models in its activation.⁴⁸ Here we study the role of electrostatics in altering the conformation distributions as well as the dynamics of Ca^{2+} –CaM using extensive MD simulations starting from its extended and compact forms under standard protonation states (3CLN and 1PRW, respectively) as well as by protonating nine residues with relatively high pK_a values (3CLN*). For 3CLN and 1PRW, the N-lobe, C-lobe and the linker maintain their local stability. As confirmed by rmsd profiles (Figure 1), the dominant modes of motion (Figure 4 and Table 1) and the relative orientations of the lobes quantified by (θ, φ) maps (Figure 3), these structures are energetically stable and sample conformations in a local energy minimum. Our observations are also consistent with experimental studies which predict conformational switching occurring on 100 μs time scale.¹⁵

Our previous PRS work on CaM suggested that external perturbations on acidic residues with elevated pK_a values may cause the conformational change.¹¹ In fact, altering the protonation state of residues which are highly sensitive to pH changes in 3CLN* readily leads to a conformational switch to a more compact form on sub-100 ns time scales. The structure is compatible with the FRET results both in terms of the interlobe distances and the fact that lowering the pH to 5.0 leads to a single stable state as opposed to the presence of at least two distinct forms at 7.4 pH. The final, equilibrated structure is also similar to several ones from the ensemble of conformations representing the structure and dynamics of Ca^{2+} –CaM as related to NMR derived parameters.⁴⁹

Our current view suggests that at high pH, barrier crossing to the compact form is prevented by the repulsive electrostatic interactions between the two lobes at physiological pH. Because of the remote location of the oppositely charged patches on the two domains, the conformational change only occurs when a simultaneous torsion and bending of the two lobes with respect to each other takes place, a rare event occurring on 100 μs time scales. Lowering the pH significantly alters the charge distribution on the protein surface, leading to a change in the overall conformational landscape. Thus, even at elevated pH, the protein might ease the passage between the different conformers by acquiring protons from the solvent environment. It is interesting to note that these residues with elevated pK_a values are also strategically located at regions of the protein which may mechanically induce allosteric changes.¹¹ Adaptation to different pH values in various subcellular compartments is thought to be directly related to protein stability⁵¹ and pH of optimal binding affinity of interacting proteins.⁵² Methods to determine how proteins adapt to cellular and subcellular pH are currently sought-after⁵³ and the

current study contributes to the knowledge-base in this direction.

■ ASSOCIATED CONTENT

■ Supporting Information

Table S1 listing the calculated pK_a values of all ionizable residues and Figures S1–S3 summarizing the results from the second 3CLN* depicting repeatability of the observed conformational change. This material is available free of charge via the Internet at <http://pubs.acs.org>.

■ AUTHOR INFORMATION

Corresponding Author

*E-mail: canan@sabanciuniv.edu. Phone: +90 (216) 483 9523. Fax: +90 (216) 483 9550.

Notes

The authors declare no competing financial interest.

■ ACKNOWLEDGMENTS

This work was supported by the Scientific and Technological Research Council of Turkey Project (grant 110T624). SN is supported by a Turkish Academy of Sciences postdoctoral grant.

■ REFERENCES

- (1) Shi, C.; Wallace, J. A.; Shen, J. K. *Biophys. J.* **2012**, *102*, 1590.
- (2) Ikura, M.; Ames, J. B. *Proc. Natl. Acad. Sci. U.S.A.* **2006**, *103*, 1159.
- (3) Fallon, J. L.; Quijcho, F. A. *Structure* **2003**, *11*, 1303.
- (4) Vondonselaar, M.; Hickie, R. A.; Quail, J. W.; Delbaere, L. T. J. *Nat. Struct. Biol.* **1994**, *1*, 795.
- (5) Junker, J. P.; Rief, M. *Proc. Natl. Acad. Sci. U.S.A.* **2009**, *106*, 14361.
- (6) Atilgan, C.; Atilgan, A. R. *PLoS Comput. Biol.* **2009**, *5*.
- (7) Ikeguchi, M.; Ueno, J.; Sato, M.; Kidera, A. *Phys. Rev. Lett.* **2005**, *94*.
- (8) Atilgan, C.; Gerek, Z. N.; Ozkan, S. B.; Atilgan, A. R. *Biophys. J.* **2010**, *99*, 933.
- (9) Gerek, Z. N.; Ozkan, S. B. *PloS Comput. Biol.* **2011**, *7*.
- (10) Baysal, C.; Atilgan, A. R. *Proteins: Struct., Funct., Genet.* **2001**, *43*, 150.
- (11) Atilgan, A. R.; Aykut, A. O.; Atilgan, C. J. *Chem. Phys.* **2011**, *135*, 15.
- (12) Atilgan, C.; Okan, O. B.; Atilgan, A. R. *Annu. Rev. Biophys.* **2012**, *41*, 205–225.
- (13) Bertini, I.; Del Bianco, C.; Gelis, I.; Katsaros, N.; Luchinat, C.; Parigi, G.; Peana, M.; Provenzano, A.; Zoroddu, M. A. *Proc. Natl. Acad. Sci. U.S.A.* **2004**, *101*, 6841.
- (14) Slaughter, B. D.; Allen, M. W.; Unruh, J. R.; Urbauer, R. J. B.; Johnson, C. K. *J. Phys. Chem. B* **2004**, *108*, 10388.
- (15) Price, E. S.; DeVore, M. S.; Johnson, C. K. *J. Phys. Chem. B* **2010**, *114*, 5895.
- (16) Wilson, M. A.; Brunger, A. T. *J. Mol. Biol.* **2000**, *301*, 1237.
- (17) Babu, Y. S.; Bugg, C. E.; Cook, W. J. *J. Mol. Biol.* **1988**, *204*, 191.
- (18) Wriggers, W.; Mehler, E.; Pitici, F.; Weinstein, H.; Schulten, K. *Biophys. J.* **1998**, *74*, 1622.
- (19) Yang, C.; Jas, G. S.; Kucera, K. J. *Biomol. Struct. Dyn.* **2001**, *19*, 247.
- (20) Fiorin, G.; Biekofsky, R. R.; Pastore, A.; Carloni, P. *Proteins: Struct., Funct., Bioinf.* **2005**, *61*, 829.
- (21) Barbato, G.; Ikura, M.; Kay, L. E.; Pastor, R. W.; Bax, A. *Biochemistry* **1992**, *31*, 5269.
- (22) Likic, V. A.; Gooley, P. R.; Speed, T. P.; Strehler, E. E. *Protein Sci.* **2005**, *14*, 2955.
- (23) VanderSpoel, D.; DeGroot, B. L.; Hayward, S.; Berendsen, H. J. C.; Vogel, H. J. *Protein Sci.* **1996**, *5*, 2044.
- (24) Chakrabarti, B.; Levine, A. J. *Phys. Rev. E* **2006**, *74*, 031903.
- (25) Project, E.; Friedman, R.; Nachliel, E.; Gutman, M. *Biophys. J.* **2006**, *90*, 3842.
- (26) Yang, L. J.; Gao, Y. Q. *J. Phys. Chem. B* **2007**, *111*, 2969.
- (27) Shepherd, C. M.; Vogel, H. J. *Biophys. J.* **2004**, *87*, 780.
- (28) Crivici, A.; Ikura, M. *Annu. Rev. Biophys. Biomol. Struct.* **1995**, *24*, 85.
- (29) Berman, H. M.; Westbrook, J.; Feng, Z.; Gilliland, G.; Bhat, T. N.; Weissig, H.; Shindyalov, I. N.; Bourne, P. E. *Nucleic Acids Res.* **2000**, *28*, 235.
- (30) Phillips, J. C.; Braun, R.; Wang, W.; Gumbart, J.; Tajkhorshid, E.; Villa, E.; Chipot, C.; Skeel, R. D.; Kale, L.; Schulten, K. *J. Comput. Chem.* **2005**, *26*, 1781.
- (31) Humphrey, W.; Dalke, A.; Schulten, K. *J. Mol. Graphics* **1996**, *14*, 33.
- (32) Brooks, B. R.; Bruccoleri, R. E.; Olafson, B. D.; States, D. J.; Swaminathan, S.; Karplus, M. *J. Comput. Chem.* **1983**, *4*, 187.
- (33) Darden, T.; Perera, L.; Li, L. P.; Pedersen, L. *Struct. Folding Des.* **1999**, *7*, R55.
- (34) Andersen, H. C. *J. Comput. Phys.* **1983**, *52*, 24.
- (35) Gordon, J. C.; Myers, J. B.; Foltz, T.; Shoja, V.; Heath, L. S.; Onufriev, A. *Nucleic Acids Res.* **2005**, *33*, W368.
- (36) Myers, J.; Grothaus, G.; Narayanan, S.; Onufriev, A. *Proteins* **2006**, *63*, 928.
- (37) Connolly, T.; B.M.; Nielsen, J. *Nucleic Acids Res.* **2006**, W48–51.
- (38) Connolly, T.; B.M.; Nielsen, J. *Protein Sci.* **2007**, *16*, 239.
- (39) Rostkowski, M.; Olsson, M. H. M.; Sondergaard, C. R.; Jensen, J. H. *BMC Struct. Biol.* **2011**, *11*, 6.
- (40) Kantardjiev, A. A.; Atanasov, B. P. *Nucleic Acids Res.* **2009**, *37*, W422.
- (41) Project, E.; Nachliel, E.; Gutman, M. *J. Comput. Chem.* **2008**, *29*, 1163.
- (42) Project, E.; Nachliel, E.; Gutman, M. *J. Comput. Chem.* **2010**, *31*, 1864.
- (43) Slaughter, B. D.; Bieber-Urbauer, R. J.; Johnson, C. K. *J. Phys. Chem. B* **2005**, *109*, 12658.
- (44) Okan, O. B.; Atilgan, A. R.; Atilgan, C. *Biophys. J.* **2009**, *97*, 2080.
- (45) Chou, J. J.; Li, S. P.; Klee, C. B.; Bax, A. *Nat. Struct. Biol.* **2001**, *8*, 990.
- (46) Dasgupta, S.; Hu, X. Y.; Keizers, P. H. J.; Liu, W. M.; Luchinat, C.; Nagulapalli, M.; Overhand, M.; Parigi, G.; Sgheri, L.; Ubbink, M. *J. Biomol. NMR* **2011**, *51*, 253.
- (47) Bertini, I.; Giachetti, A.; Luchinat, C.; Parigi, G.; Petoukhov, M. V.; Pierattelli, R.; Ravera, E.; Svergun, D. I. *J. Am. Chem. Soc.* **2010**, *132*, 13553.
- (48) Anthis, N. J.; Doucleff, M.; Clore, G. M. *J. Am. Chem. Soc.* **2011**, *133*, 18966.
- (49) Gsponer, J.; Christodoulou, J.; Cavalli, A.; Bui, J. M.; Richter, B.; Dobson, C. M.; Vendruscolo, M. *Structure* **2008**, *16*, 736.
- (50) Ikura, M.; Clore, G. M.; Gronenborn, A. M.; Zhu, G.; Klee, C. B.; Bax, A. *Science* **1992**, *256*, 632.
- (51) Chan, P.; Warwicker, J. *BMC Biol.* **2009**, *7*, 69.
- (52) Zhang, Z.; Witham, S.; Alexov, E. *Phys. Biol.* **2011**, *8*, 3.
- (53) Garcia-Moreno, B. J. *Biol.* **2009**, *8*, 98.1.